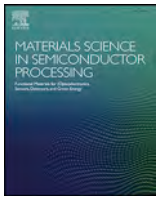
Materials Science in Semiconductor Processing 200 (2025) 109929



Contents lists available at ScienceDirect

Materials Science in Semiconductor Processing

journal homepage: www.elsevier.com/locate/mssp



Formation of silicon nitride by high-fluence femtosecond laser treatment

Alex T. Sheardy *, Botond Santa, Svetlana Neretina, Justin T. Krantz, Maksym A. Zhukovskyi, Edward C. Kinzel, Karel Matouš, Alexander S. Mukasyan

University of Notre Dame, Notre Dame, IN, 46556, USA

ARTICLE INFO

Keywords:
Femtosecond laser
Irradiation
Silicon nitrogen system
Silicon nitride formation

ABSTRACT

High-fluence femtosecond laser pulses can induce physical and chemical changes in materials that are unrealizable under standard laboratory conditions. The exact nature of these changes can depend strongly on the gaseous environment in which the material is irradiated since near-surface chemical reactions can occur between the two materials. Surface modifications of silicon are of particular interest due to its significance in semiconductor-based applications. Specifically, the formation of silicon nitride (Si_3N_4) structures is desirable for multiple applications due to its high stability and low dielectric constant. Herein, we report on femtosecond laser-induced morphological and chemical modifications of silicon in a nitrogen atmosphere. We observed an extremely fast chemical reaction in the silicon-nitrogen system. The presence of crystalline Si_3N_4 was confirmed using high-resolution transmission electron microscopy, representing the first reported synthesis of Si_3N_4 nanocrystals through femtosecond laser-based methods. In addition, the surface was found to contain alternating layers of amorphous and crystalline silicon. Provided are plausible mechanisms for the formation of each of these structures. Taken together, these findings on surface modification of silicon using femtosecond laser irradiation may provide new pathways for manufacturing of nanoscale devices.

1. Introduction

Femtosecond laser irradiation is a powerful tool for inducing physical and chemical transformations which are otherwise unfeasible in a typical laboratory setting through the use of ultrashort laser pulses ($\sim 10^{-15}$ s) that generate non-equilibrium conditions within a target material [1]. The high energy of the laser pulses can excite molecular vibrations, rotations, and electronic transitions, leading to the rapid rearrangement of the atomic bonds and the subsequent formation of new chemical species. Femtosecond laser irradiation can also lead to the generation of highly reactive species such as radicals and ions, which can significantly accelerate chemical interactions. It is well-recognized that these reactions have the potential to be applied in a wide range of fields including photochemistry, materials science, and organic synthesis [2]. However, there is remains a lack of experimental data on fs-laser irradiation chemistry to allow for a full-understanding of these short-duration interactions.

Most prior research on the subject focused on surface modifications as well as the formation of various coatings [3,4]. For example, fs-lasers were exploited to modify the surface properties of refractory materials such as titanium nitride, titanium carbide (TiC), and silicon carbide (SiC) [5–11]. The so-formed surfaces possess superior tribological properties, reduced friction, and/or enhanced biocompatibility. In addition, fs-lasers have been utilized in the synthesis and deposition of nanoparticles and films on various substrates including silicon (Si) [12,13]. Silicon under femtosecond laser irradiation is a topic that has gained significant interest in recent years due to its potential applications in various fields such as microelectronics, photonics, and optoelectronics. One of the key advantages of femtosecond laser irradiation as it relates to silicon is the ability to generate precise, high-resolution patterns over the surface of the material. This has led to its use in the fabrication of micro- and nanoscale devices such as photonic crystals, waveguides, and sensors [14–19].

Silicon nitride (Si_3N_4) is a unique and versatile material whose significance in the semiconductor industry stems from functionalities that include passivation, insulation, diffusion barriers, and dielectric layers [20,21]. It is also used in the production of micro-electromechanical systems (MEMS) devices, sensors, and protective coatings [22–25]. One of the key benefits of silicon nitride layers is their excellent thermal and chemical stability, making them ideal for use in high-temperature and chemically harsh environments. With a low dielectric constant, these layers are also well-suited for use in integrated circuits and other

* Corresponding author.
E-mail address: asheardy@nd.edu (A.T. Sheardy).

https://doi.org/10.1016/j.mssp.2025.109929
Received 29 May 2025; Received in revised form 24 July 2025; Accepted 3 August 2025
Available online 6 August 2025
1369-8001/© 2025 The Authors. Published by Elsevier Ltd. This is an open access article under the CC BY license (http://creativecommons.org/licenses/by/4.0/).

electronic devices where minimizing signal interference is critical.

To our knowledge, the use of fs laser irradiation to synthesize solid Si_3N_4 has not heretofore been reported. There are, however, several studies investigating such interactions in the silicon-carbon and titanium-nitrogen systems [26–31]. A silicon carbide phase was detected during the fabrication of Si nanoparticles by fs (35–900 fs) laser ablation of a single-crystal silicon wafer immersed in 95 % ethanol. While the main products were Si nanoparticles in the size range of 20–150 nm, HRTEM also detected a small quantity of SiC nanocrystals with sizes greater than 5 nm [26]. It is worth noting that significantly more β−SiC nanoparticles with sizes of approximately 3.5 nm were detected when using a 10 ns laser in a similar experimental configuration [27]. In the latter case, the reaction time was estimated to be 10^3 ns. Fs-laser (700 fs) ablation of a Si wafer immersed in hexane also resulted in the formation of a mixture of Si (major component) and SiC nanoparticles [28]. For this case, the size of the carbide particles was considerably larger (100–200 nm), and particles with sizes exceeding 100 nm possessed a Si-SiC core-shell morphology. Silicon carbide nanocrystals, with sizes ranging from 70 to 700 nm, have also been synthesized by irradiating a carbon layer (2.5 μm) deposited on a silicon wafer with 42 fs laser pulses at a repetition rate of 1 kHz [29]. The number of shots was varied in the range of 50–3000 with laser fluences of 0.23–1.15 J/cm^2, all of which are well above the ablation threshold of carbon and silicon. SiC crystals were only observed after 3000 shots when using an intermediate fluence of 0.63 J cm^{-2}.

Titanium nitride and oxy-nitride phases were detected on a titanium surface after fs-laser irradiation in a nitrogen atmosphere. The titanium foil was irradiated in nitrogen flow (2.5 L min^{-1}) with 10^4 fs-laser pulses (wavelength 1040 nm, pulse length 350 fs, spot size ~ 40 mm, fluence 1–1.6 J cm^{-2}) [30]. It was observed that the amount of TiN on the surface increased as the fluence increased. In addition, cleaning of the Ti surface by irradiation in argon led to a further enhancement in surface nitridation. Even then, the total concentration of the nitride on the surface did not exceed 9 at.%. Another study reported on the interaction of titanium with nitrogen gas under laser irradiation where a high power (100 W), high pulse repetition rate (1 MHz) fs-laser was used ($\lambda = 1030$ nm, $\tau = 750$ fs, fluence ~ 0.5 J cm^{-2}, N = 250) [31]. In this nitrogen atmosphere, a homogeneous TiON coating was formed. EDX analysis revealed 17 at.% of nitrogen on the surface layer. Parameters of relevance for all of the aforementioned studies are summarized in Table S1.

Herein, we report on the chemical interaction between a Si wafer and nitrogen during fs-laser irradiation (290 fs) with a few high-fluence pulses (~100 J cm^{-2}) where specific attention is paid to the structural and phase transformations that take place on the atomic level. Specifically, we observed the formation of sequences of crystal-amorphous silicon layers and silicon nitride crystals. These findings may provide a foundation for future work towards the fabrication of various nanoscale devices.

2. Methods

The experiments were performed in a custom-built pressure vessel rated for 10 atm and able to accept various gases. The laser source used was a Pharos PH1-20 W fs laser with a pulse duration of 290 fs and a center wavelength of 1030 nm. The pulse energy and repetition rate were set to E = 200 μJ and f = 10 kHz, respectively. The laser is directed through a fused quartz (FQ) window onto the focal plane by a scan head (ScanLABS exceliSCAN 14) to a nominal spot diameter of 15 μm to attain a peak fluence of 226 J cm^{-2}.

A polished p-type (100) Si single-crystal wafer (MTI Corporation, USA) was loaded into the pressure vessel and pumped to a base pressure of 0.04 atm. The vessel was then filled to 1 atm with high-purity Ar gas where a slight overpressure allowed for a continuous flow through an outlet that, over time, purged residual oxygen from the system. For laser exposures carried out under a nitrogen atmosphere, the Ar gas was first purged from the system with high-purity N_2 gas while maintaining an overpressure of 1.05 atm. The oxygen content was monitored and stayed below the detection limit of 200 ppm for the duration of the process. The laser beam is positioned in the XY-plane by a Galvo scanner and focused onto the surface of the substrate using a f-theta lens. The beam was scanned along 500 μm diameter circular paths with varying speeds (v_s: 22.2, 40, 100, and 200 mm/s) to avoid issues associated with the shuttering of the beam. A schematic of the experimental setup is provided in Fig. 1.

The morphological characteristics of the laser-irradiated materials were examined using a field emission scanning electron microscope (FESEM, Magellan 400, Thermo Fisher Scientific Inc., USA) equipped with an energy-dispersive X-ray spectroscopy (EDX) system (Bruker, USA). EDX mapping was performed to investigate the distribution of nitrogen within the treated sample. These maps were further used to identify areas of high nitrogen content for preparation of lamella for transmission electron microscopy (TEM). TEM samples were prepared in a Helios G4 Ux Dual Beam SEM (Thermo Fisher Scientific, USA) through focused ion beam (FIB) etching utilizing a standard lift-out technique. High-resolution images were captured using a double-tilt holder on a Talos F200i TEM (Thermo Fisher Scientific, USA) operated at 200 kV. STEM images were taken using a Panther STEM detector system in high-angle annular dark field (HAADF) mode. Compositional analysis was conducted in STEM mode using energy dispersive X-ray spectroscopy (EDX, SuperX detector, Thermo Fisher Scientific, USA). Selected area electron diffraction (SAED) was used to analyze the crystal structure of the treated material. Electron energy loss spectroscopy (EELS) was performed using the GIF unit of a Continuum K3 system (Gatan, USA) equipped on a Spectra 300 STEM (Thermo Fisher Scientific, USA)

3. Results

As a control, a TEM lamella from an untreated Si single-crystal substrate was prepared and imaged (Fig. S1a and b). The cross section reveals a 2–3 nm thick silicon oxide layer on the surface of the crystal (Fig. S1c–f) where the Ir, C, and Pt layers all originate from SEM-FIB sample preparation. After laser irradiation, a 3D structure appeared on the Si surface that was analyzed using an optical surface profiler (Zygo NewView 9000, AMETEK Inc., USA). Fig. 2 shows the optical intensity maps obtained for irradiated surfaces with different scan speeds. Despite the nominal laser spot diameter of 15 μm, the high pulse energy results in an area ~50 μm in diameter with sufficient energy to cause ablation and/or surface modification. This resulted in overlapping modified areas, with the fastest speed giving the least overlap and the slowest scan speed resulting in significant overlap. By using the scan speed, beam path diameter, ablated area size, and repetition frequency, the number of overlapping spots can be estimated. With the fastest scan speed, there are 1–3 overlapping pulses, while the slowest scan speed gives a maximum of ~23 overlapped pulses. Regardless of scan speed, there is generally more overlap in the middle of the annulus, and less at the edges.

The minimal overlap result (200 mm/s scan speed) exhibits a laser-induced periodic surface structure that is typical for a femtosecond laser interaction with Si. As the scan speed is decreased, overlap increases and the ablation effects become more pronounced (panels b–d). Consequently, several micron-deep trenches emerge with rough surfaces along with a considerable amount of debris that is located in the immediate vicinity. An example of the analysis performed for the fastest scan (v_s = 200 mm/s) experiment is shown in Fig. 3a. Fig. 3b shows representative profiles for the structures obtained under the various spot overlap conditions. SEM and EDX were used to characterize the surface topology and composition of the laser-irradiated areas (Fig. S2). A comparison of the minimal and maximal overlap samples reveals the emergence of a deepening cavity that is accompanied by an increased nitrogen signal that appears in the EDX spectra as a low-energy shoulder on the oxygen peak (Fig. S2). EDX mapping of the maximal overlap sample reveals that the concentration of both oxygen and nitrogen is highest outside of the

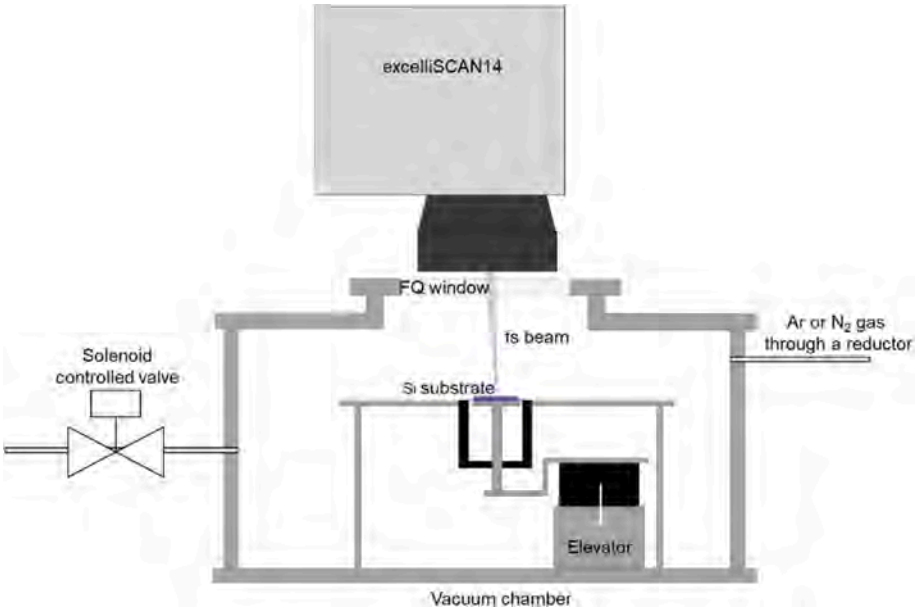


Fig. 1. Schematic of the experimental setup used in the laser-based synthesis of Si_3N_4 wherein a Si substrate irradiated in N_2 atmosphere.

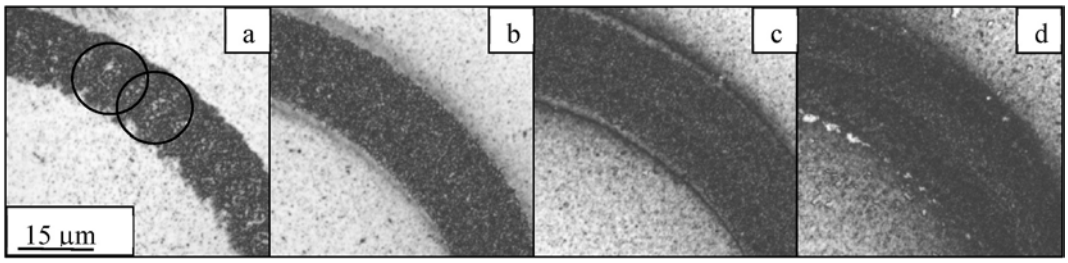


Fig. 2. Optical intensity maps of the Si surface after its irradiation with a 200 µJ laser beam with scan speeds of (a) v_s = 200; (b) 100; (c) 40; and (d) 22.2 mm/s.

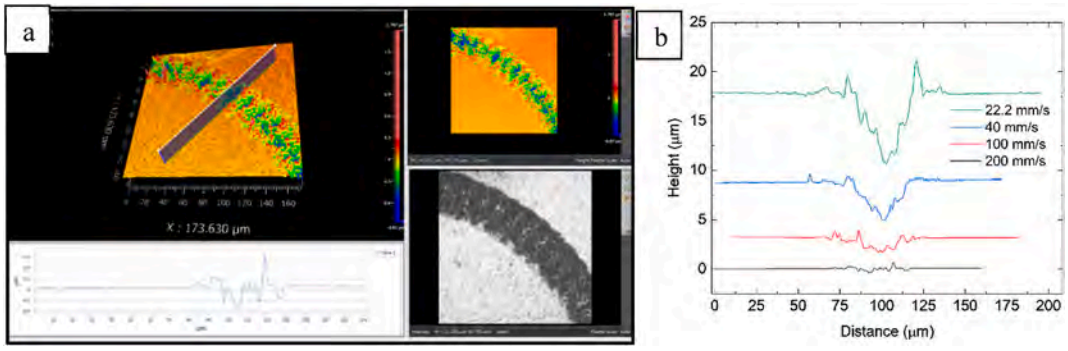


Fig. 3. (a) Cross section of the laser irradiated area obtained using a 3D surface profiler under the fastest scan speed. (b) Profiles obtained for all laser scan speeds.

direct beam path and lower within the beam path. Additionally, EDX point analysis shows nitrogen content at ~25 % in specific nitrogen-rich regions (Fig. S2). TEM lamella were prepared from regions showing the highest nitrogen content, near the boundary of the irradiated zone.

TEM characterization for the sample with the fastest scan speed is presented in Fig. 4. Recall that all investigated specimens represent the characteristic structures, which was proven by multiple samples cross sectioning in the areas with maximum nitrogen concentration (EDS data). Fig. 4a reveals that the unirradiated area (*i.e.*, left side) remains morphologically unchanged whereas the irradiated area (*i.e.*, right side) shows a significant transformation. Low magnification EDX was used to survey the large protrusion (denoted by red box in Fig. 4a). The images (Fig. 4b and c) show that it consists of Si with an oxygen-rich surface layer. This surface layer also appeared to be porous as carbon and platinum contaminants from the FIB deposition were detected. Close inspection of the surface layer also exposed the presence of nitrogen (Fig. 4d and e), potentially indicating the formation of silicon oxynitride. It is important to note that Si_3N_4 was not observed in the sample. The EDX spectrum of this region, which is provided in Fig. S3a, clearly shows the presence of both O and N. Fast Fourier transform (FFT) analysis (Fig. 4f inset) identified the crystalline regions marked in red as Si. From this image, it is apparent that an amorphous Si layer exists between two crystalline Si layers. No other crystalline phases were observed, indicating that any silicon oxynitride phase would have to be

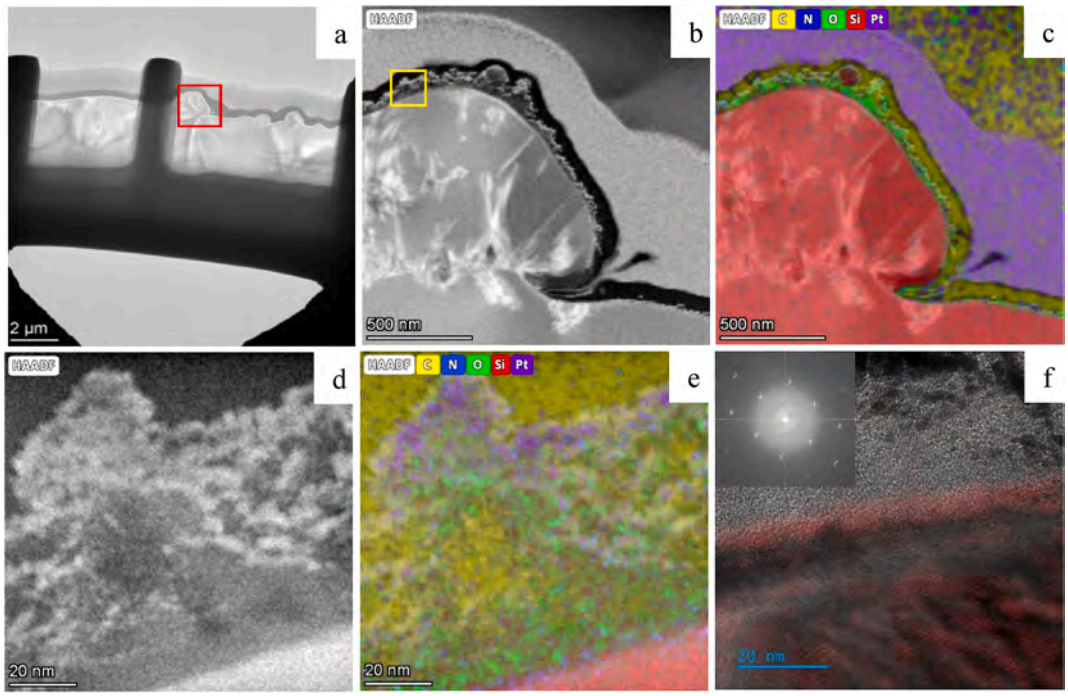


Fig. 4. (a) BF-TEM and (b) HAADF-STEM micrographs for a laser-irradiated sample prepared under the fastest laser scan conditions along with the (c) associated low-magnification C, N, O, Si, and Pt wt.% EDX-STEM mapping. Higher magnification (d) HAADF, (e) wt.% EDX, and (f) HRTEM micrographs for the surface of the protrusion denoted by the yellow box in (b). The inset in (f) is the FFT of the image, showing single-crystal silicon. Scale bars are 2 μm (a), 500 nm (b–c) and 20 nm (d–f).

amorphous.

Fig. 5 presents images and elemental mapping obtained for a lamella prepared from a sample laser-irradiated at the slowest scan speed. The HAADF-STEM micrograph (Fig. 5a) shows that significant morphological change has occurred. HAADF- and EDX-STEM (Fig. 5b and c) were performed on the protrusion denoted by the red box in Fig. 5a. Within this protrusion, two areas were analyzed (Fig. 5c): One internal area showing higher nitrogen content (Area 1, yellow box) and another area near the surface of the Si (Area 2, blue box). It is worth noting that the EDX map is presented as weight-percentage and the mapping software attempts to fill all areas, including voids.

A HAADF-STEM micrograph of Area 1 is shown in Fig. 6a and corresponding EDX mapping in Fig. 6b. EDX mapping allowed for clear identification of the region with higher N content. A profile along this N-rich region was taken (Fig. 6c) and gives atomic percentages of 55.1 % N and 44.9 % Si, consistent with the percentages expected for Si_3N_4 (*i.e.,* 57 % N and 43 % Si). To confirm, HRTEM was performed to investigate the crystal structure (Fig. 6d and e). The HRTEM image (Fig. 6d) contains two distinct crystal structures, as shown in the FFT (Fig. 6e). Most reflections correspond to Si, however the reflections circled in blue represent a lattice with spacing of 3.8 Å, which fits well with the (110) plane of either α- or β-Si_3N_4. Mapping the crystal spacings back onto the original images (Fig. 6d), results in the colored mapping where blue corresponds to the 3.8 Å Si_3N_4 (110) plane and red corresponds to the 2.69 and 3.10 Å Si (002) and (111) planes, respectively. It is worth noting that the blue region with the 3.8 Å spacing overlaps with the N-rich region measured by EDX (Fig. 6b), further confirming the presence of a Si_3N_4 phase. It should also be noted that the area below the Si_3N_4 inclusion is amorphous and shows only Si. The EDX spectrum for this region is presented in Fig. S3b and a higher magnification of the Si_3N_4 crystal is presented in Fig. S4.

To address the viability of this method to produce silicon nitride, an additional lamella was prepared from a second sample treated under the same experimental conditions. Within this lamella, several Si_3N_4 inclusions were observed as shown by EDX (Fig. S5). Selected area electron diffraction (SAED) was collected to demonstrate that the Si_3N_4 was in the α-phase (Fig. S6). This conclusion is based off the strong agreement of multiple diffraction spots, and that a diffraction spot at 4.31 Å is

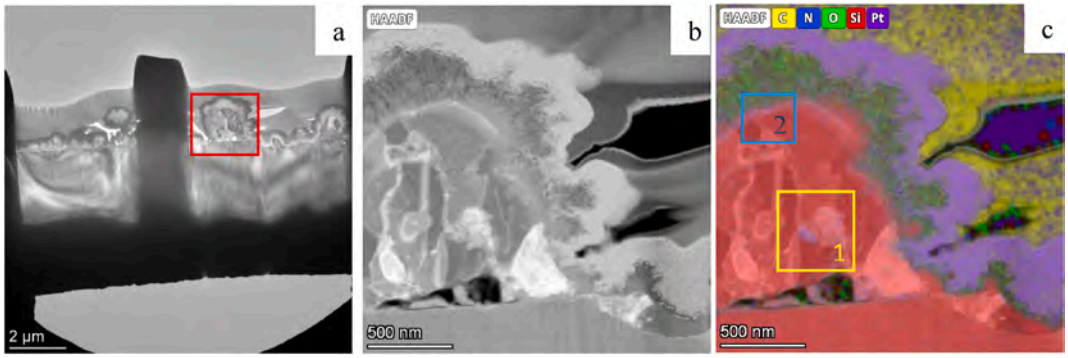


Fig. 5. (a) BF-TEM image; (b) HAADF and (c) corresponding low magnification C, N, O, Si, Pt wt.% EDX-STEM mapping for the sample prepared under the slowest laser scan conditions. Scale bars are 2 μm (a) and 500 nm (b–c).

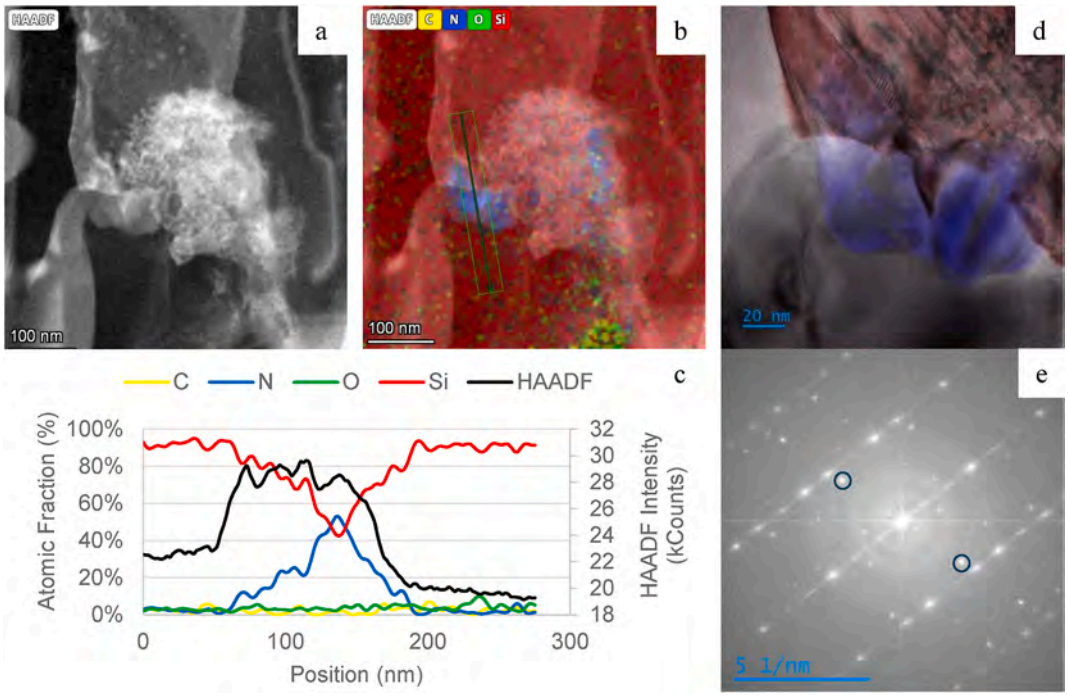


Fig. 6. (a) HAADF- and (b) at.% EDX-STEM of Area 1 from Fig. 4. (c) The elemental composition along the line profile marked in Fig. 6b. (d) HRTEM focused on the nitrogen-rich area in Fig. 6b, where the red and blue areas have lattice spacing corresponding to Si and α- or β-Si_3N_4, respectively. (e) FFT of Fig. 6d where the reflections circled in blue are assigned to Si_3N_4. Scale bars are 100 nm (a–b), 20 nm (d) and 5 nm^{-1} (e).

expected for the (101) plane in α-Si_3N_4 while no planes have similar d-spacing in Si, β-, or γ-Si_3N_4. To further confirm the synthesis of Si_3N_4, electron energy loss spectroscopy (EELS) was performed on both a nitrogen-rich area and the unaltered substrate (Fig. S7). The first energy-loss near-edge structure (ELNES) peak for the nitrogen-rich area is shifted by ~5 eV as compared to silicon. Additionally, the second ELNES peak is much narrower for the nitrogen-rich area as compared to the substrate. The same trends were observed by Worch et al., and the spectra show strong agreement overall [32].

HAADF- and EDX-STEM micrographs of Area 2 are presented in Fig. 7a and b. A line profile through this interface region shows a general trend of increasing Si and decreasing C, N, and O (Fig. 7c). The presence

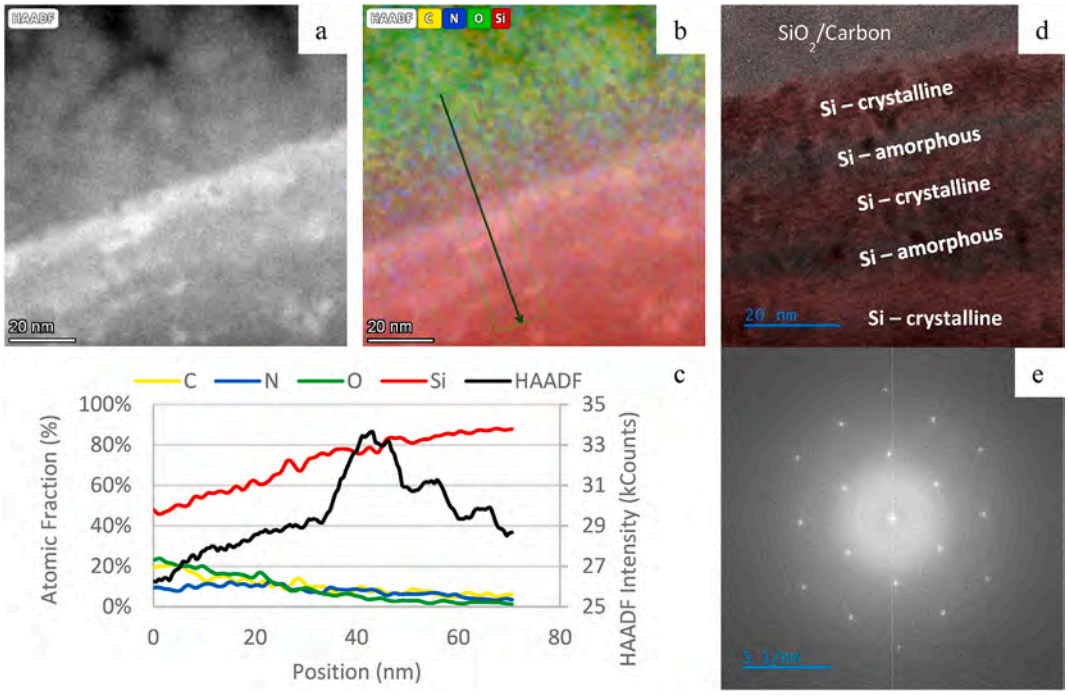


Fig. 7. (a) HAADF- and (b) wt.% EDX-STEM of Area 2 from Fig. 4c. (c) The elemental composition along the line profile marked in Fig. 7b. (d) HRTEM focused on the nitrogen-rich area in Fig. 7b.The red marked areas have lattice spacing corresponding to Si. (e) FFT of Fig. 7d, with all reflections corresponding to single-crystal Si. Scale bars are 20 nm (a-b, d) and 5 nm^{-1} (e).

of Si, O, N, and C in the top layer may be the result of porous silica or silicon oxynitride that formed during or after the laser irradiation, with carbon depositing into the pores during FIB sample preparation. An EDX spectrum of this region is presented in Fig. S3c. A more interesting phenomenon is observed in the HRTEM micrograph of this region (Fig. 7d). While the FFT (Fig. 7e) represents only single-crystal silicon, mapping the crystalline regions shows non-uniformity (Fig. 7d). The uppermost region is an amorphous, porous oxynitride into which carbon penetrated during deposition. Below this is a four-layer structure that alternates between crystalline and amorphous Si with layer thicknesses of 15, 5, 20, and 5 nm. Finally, at the bottom is bulk crystalline Si.

4. Discussion

Taken together, the reported data shows two important effects occurring when Si is irradiated with multiple fs laser pulses in a nitrogen atmosphere: (i) the formation of crystalline Si_3N_4 and (ii) a multilayer structure alternating between crystalline and amorphous phases of Si that occurs near the surface of the irradiated area. Hypotheses for the origin of these effects are discussed separately.

Formation of Silicon Nitride. The silicon – nitrogen system involves several specific features needed to analyze the mechanism of silicon nitride formation. First, the solubility of nitrogen in silicon, including molten silicon, is extremely low. At the melting point of Si (1687 K), solubility is limited to $C_N = 42$ ppm by mass, which slowly increases with temperature according to [33]:

$$C_N(T) = 7958 * e^{-\frac{24376}{T}} \ (T: 1687 - 1832\ K)$$

Second, the equilibrium phase diagram (see Fig. S8) reveals that bulk silicon nitride exists only in the Si_3N_4 stoichiometry and that it dissociates to liquid silicon and gas nitrogen at a critical temperature of near 2200 K at 1 atm of nitrogen [34]. The dissociation temperature slowly increases with increasing nitrogen pressure (see Fig. S9) [35]:

$$T_d = \frac{880728}{411.14 - 8.314 * \ln\left(P_{N_2}^2\right)}$$

Third, there are three crystallographic structures of Si_3N_4, designated as α, β and γ phases [36]. The α (trigonal, P31c) and β (hexagonal, $P6_3/m$) phases are the most common forms of Si_3N_4 and can be produced under standard pressure conditions. Cubic γ-Si_3N_4 (F $\bar{d}$ 3m) has a spinel-type structure and can only be synthesized under high pressures (*i.e.,* P > 20 GPa) [37]. Fourth, due to the extremely low solubility of nitrogen in silicon and the high energy of nitride formation (*i.e.,* 760–829 kJ mol^{-1}), the reaction rates are low and nuclei formation is a limiting stage [38]. The typical reaction time between silicon and nitrogen can vary depending on the specific reaction conditions (*e.g.*, temperature, pressure, presence of catalysts, *etc.*). In general, the formation of silicon nitride from Si and N_2 typically takes place at high temperatures (*i.e.*, 1400–1800 °C) and can take anywhere from a few hours to several days to complete. However, use of high-energy methods like plasma can cause the reaction to occur much more quickly. For example, the β-Si_3N_4 phase was formed in 1 s by using a self-sustained reaction carried out at 2000 K and a gas pressure of 10 MPa [39,40].

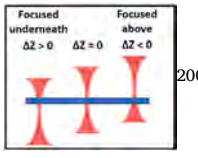
While there is limited experimental data on the Si-N_2 interaction under laser irradiation conditions, modeling of chemical reactions in laser-induced Si-N plasma has been performed [41]. The main findings are that (i) shockwaves in laser-induced Si-N plasmas have no effect on chemical reactions, (ii) chemical bonding only occurs in the plume boundary layer where a high temperature gradient exists after the shockwaves have dissipated, (iii) the thickness of this boundary layer increases with time because the slope of the temperature drop becomes smaller due to plume expansion, and (iv) the expansion of the hot region of the plasma plume slows down and practically stops after about 3 μs. Additionally, typical plasma compositions as a function of temperature for different Si:N mole ratios were calculated (Fig. S10). These simulated results suggest that silicon and nitrogen predominantly exist as free radicals in plasmas at temperatures of 10,000 K, but small quantities of diatomic gaseous SiN are also present. Recent experiments have also confirmed the formation of diatomic SiN gaseous molecules in laser-induced plasma [42]. Taken together, this suggests that the SiN^0 molecules could serve as nucleation sites for growth via either gas/-plasma or condensed phase reactions. The low concentration of the SiN^0 species can further explain the small concentration of obtained Si_3N_4.

To estimate the characteristic time-scales, computational two-temperature modeling of femtosecond laser heating of a Si wafer was performed (see Supplementary Information). For the simulation, a silicon wafer of radius 100 μm and thickness 100 μm was used. The laser parameters, constant material properties, variable material properties and time steps are provided in Table S2–S5. For each time segment, the maximum electron temperature, lattice temperature, and charge carrier density was calculated as a function of time (Fig. S11). The electron density reaches a saturation point of $5 \times 10^{28}\ m^{-3}$ before the peak laser intensity reached at approximately −240 fs. Initially, the electron temperature rises rapidly and reaches a peak of $\sim 9.2 \times 10^5$ K at −390 fs before increasing again to a peak temperature of 7.3×10^7 K at 225 fs. Similar behavior was observed in the highest fluence (0.015 J/cm^2) case of Chen et al., including the initial temperature plateau followed by a second temperature increase. Finally, the electrons and lattice come into equilibrium with a temperature of $\sim 1.93 \times 10^6$ K at 15.9 ps, whereupon the system gradually cools, eventually reaching a temperature of 12,000 K at 100 μs, and then returns to room temperature (300 K) at 1 ms. The second laser pulse occurs at 100 μs, suggesting that the system has is still in a high temperature state between pulses. Additionally, the time range for chemical reactions occurring in the 1600–2200 K temperature window does not exceed 570 μs.

In the present study, the formation of Si_3N_4 inclusions after fs-laser irradiation was observed. TEM, SAED and EDX analysis reveal that the crystal structure and elemental composition fit well with those for α-Si_3N_4 phase (Fig. 6). Hence, the data suggests that the Si_3N_4 phase was formed at pressures below 20 GPa. The nitride grains were detected in the area approximately 700 nm below the surface of the specimen at a boundary between amorphous and crystalline silicon, partially immersed in both phases. Additional experiments focusing the laser above and beneath the Si surface were performed. SEM-EDX analysis of the specimen revealed that the maximum amount of nitrogen in samples occurred when the laser was focused below the Si surface (Table 1). These results suggest that while nucleation sites may form in the gas phase plasma, Si_3N_4 grain growth does not occur in the plasma but rather due to condensed phase heterogeneous chemical reactions.

The size of the observed grain is approximately 80 nm in diameter (Fig. 6). Accounting for a reaction time of approximately 570 μs and a

Table 1
EDX results for the nitrogen content as a function of the height of the focused laser spot.

E_p, μJ	Scan Speed. v_s (mm/s)	ΔZ, shift of the focus (mm)	N mass (%)	Abs. $error_{1\sigma}$, (%)
 200	100	1.2	0.00	0.07
		0.9	0.00	0.05
		0.6	0.00	0.07
		0.3	0.08	0.03
		−0.3	>0.1	N/A
		−0.9	>0.1	N/A
	40	1.2	0.19	0.03
		0.9	0.20	0.07
		0.6	**1.22**	0.07
		0.3	0.83	0.05
		−0.3	>0.1	N/A
		−0.6	>0.1	N/A
	22.2	0.6	0.83	0.05

diffusion length of 700 nm, the diffusion coefficient can be estimated as roughly $D_0 \sim 8.6 \times 10^{-6}$ cm^2 s^{-1}. This value is comparable to recently reported data on the diffusion coefficient of 1.4×10^{-5} cm^2 s^{-1} for nitrogen in molten silicon [43]. Thus nitrogen can diffuse in liquid Si for the distance observed in the experiments, but the estimated time for Si_3N_4 formation (less than 1 ms) is exceptionally low and never reported before. All of the above suggest that the silicon nitride grains formed due to chemical reaction between liquid Si and nitrogen. It is worth noting, that since Si_3N_4 exists only below the dissociation temperature 2000 K, atomic nitrogen (N^0) is not expected to contribute to the reaction, since its concentration in the plasma only becomes measurable well above this temperature (see Fig. S10) [41]. Schematics of the reaction stages are shown in Fig. S13.

Formation of Amorphous Layers. One possible explanation for the formation of the amorphous-crystalline layered structure is that these layers are formed by redeposition of material during the cooling stage. As the temperature initially decreases rapidly, there is insufficient time for the redeposited material to form ordered structures, resulting in an amorphous structure. Once the cooling rate decreases, the deposited material is able to form a crystalline phase. With each laser pulse, additional layers can be added, first amorphous and then crystalline. This can help explain the single amorphous interlayer in the minimal overlap condition, and multiple layers under the higher overlapped condition. However, given that the FFT presents a pattern for a single-crystal, this explanation is unlikely, as the redeposited layers would likely have different orientations from the initial substrate and would likely be polycrystalline.

An alternative explanation is the following: the formation of amorphous silicon layers, particularly near the outer portion of the gaussian laser pulse, has been observed in multiple reports [44,45]. Typically, these layers are formed directly on the surface of the wafer, in contrast to the present work where the amorphous layers are between crystalline layers. This difference may be due to the high fluence causing some material ablation before the amorphization occurs. A pressure/heat shockwave could then be generated below the initial surface, resulting in an amorphous layer within the material. As subsequent pulses cause more ablation, additional amorphous layers can be formed deeper within the material (see Fig. S14). Since these layers are being formed within the material, it is expected that the adjacent layers would remain unchanged (*i.e.*, single-crystalline). It should be noted that the topmost layer, which contains oxygen and nitrogen, is likely to originate from redeposition of ablated material. While regions of alternating crystalline-amorphous layers were observed in both samples, further work will seek to investigate this phenomenon in more detail.

5. Conclusion

In conclusion, this work presents two significant findings related to the surface modification of silicon when exposed to fs laser pulses in a nitrogen atmosphere: (i) the first reported synthesis of Si_3N_4 through laser irradiation of silicon, and (ii) the formation of alternating crystalline-amorphous-crystalline layers. We admit that these findings are only proof-of-concept. However, if such laser-induced modifications could be harnessed, then they would provide a pathway to controllably forming Si_3N_4 and amorphous layers for manufacturing of nanoscale semiconducting materials.

CRediT authorship contribution statement

Alex T. Sheardy: Writing – review & editing, Writing – original draft, Visualization, Methodology, Investigation, Formal analysis. **Botond Santa:** Writing – review & editing, Visualization, Methodology, Investigation. **Svetlana Neretina:** Writing – review & editing, Supervision, Methodology, Investigation, Funding acquisition, Conceptualization. **Justin T. Krantz:** Methodology, Investigation. **Maksym A. Zhukovskyi:** Writing – review & editing, Methodology. **Edward C. Kinzel:** Writing – review & editing, Supervision, Methodology, Funding acquisition, Conceptualization. **Karel Matouš:** Writing – review & editing, Methodology, Funding acquisition, Conceptualization. **Alexander S. Mukasyan:** Writing – review & editing, Writing – original draft, Supervision, Methodology, Funding acquisition, Conceptualization.

Declaration of competing interest

The authors declare that they have no known competing financial interests or personal relationships that could have appeared to influence the work reported in this paper.

Acknowledgment

S. N. acknowledges support from the National Science Foundation, Advanced Manufacturing (AM) Program, under Grant No. CMMI-2207664. This work has also benefited from the staff and facilities available through the Notre Dame Integrated Imaging Facility (NDIIF), including Ms. Tatyana Orlova who prepared the FIB lamella.

Appendix A. Supplementary data

Supplementary data to this article can be found online at https://doi.org/10.1016/j.mssp.2025.109929.

Data availability

Data will be made available on request.

References

[1] Lasers in Materials Science, Springer International Publishing, Switzerland, 2014.
[2] D. Tan, K.N. Sharafudeen, Y. Yue, J. Qiu, Femtosecond laser induced phenomena in transparent solid materials: fundamentals and applications, Prog. Mater. Sci. 76 (2016) 154–228.
[3] A.Y. Vorobyev, C. Guo, Direct femtosecond laser surface nano/microstructuring and its applications, Laser Photon. Rev. 7 (3) (2013) 385–407.
[4] K. Sugioka, Y. Cheng, Ultrafast lasers—reliable tools for advanced materials processing, Light Sci. Appl. 3 (4) (2014) e149, e149.
[5] G. Dumitru, V. Romano, H.P. Weber, M. Sentis, W. Marine, Femtosecond ablation of ultrahard materials, Appl. Phys. A 74 (6) (2002) 729–739.
[6] M.Y. Gazizova, N.A. Smirnov, S.I. Kudrayshov, V.V. Shugurov, The effect of femtosecond laser treatment on the tribological properties of titanium nitride, IOP Conf. Ser. Mater. Sci. Eng. 862 (2) (2020) 022054.
[7] Z. Zhai, C. Wei, Y. Zhang, Y. Cui, Q. Zeng, Investigations on the oxidation phenomenon of SiC/SiC fabricated by high repetition frequency femtosecond laser, Appl. Surf. Sci. 502 (2020) 144131.
[8] M.K. Kuntumalla, V.V.S.S. Srikanth, Surface patterning on nanocrystalline β-SiC thin film by femtosecond laser irradiation, Mater. Lett. 243 (2019) 136–139.
[9] B. Meng, J. Zheng, D. Yuan, S. Xu, Machinability improvement of silicon carbide via femtosecond laser surface modification method, Appl. Phys. A 125 (1) (2019) 69.
[10] J. Bonse, S.V. Kirner, R. Koter, S. Pentzien, D. Spaltmann, J. Krüger, Femtosecond laser-induced periodic surface structures on titanium nitride coatings for tribological applications, Appl. Surf. Sci. 418 (2017) 572–579.
[11] G. Dumitru, V. Romano, Y. Gerbig, H.P. Weber, H. Haefke, Femtosecond laser processing of nitride-based thin films to improve their tribological performance, Appl. Phys. A 80 (2) (2005) 283–287.
[12] J.E. Krzanowski, R.E. Leuchtner, Chemical, mechanical, and tribological properties of pulsed-laser-deposited titanium carbide and Vanadium carbide, J. Am. Ceram. Soc. 80 (5) (1997) 1277–1280.
[13] M. Vendan, P. Molian, A. Bastawros, J. Anderegg, Ultra-short pulsed laser deposition and patterning of SiC thin films for MEMS fabrication, Mater. Sci. Semicond. Process. 8 (6) (2005) 630–645.
[14] I. Pavlov, O. Tokel, S. Pavlova, V. Kadan, G. Makey, A. Turnali, Ö. Yavuz, F.Ö. Ilday, Femtosecond laser written waveguides deep inside silicon, Opt Lett. 42 (15) (2017) 3028–3031.
[15] A. Alberucci, N. Alasgarzade, M. Chambonneau, M. Blothe, H. Kämmer, G. Matthäus, C.P. Jisha, S. Nolte, In-Depth optical characterization of femtosecond-written waveguides in silicon, Phys. Rev. Appl. 14 (2) (2020) 024078.
[16] A.H. Nejadmalayeri, P.R. Herman, J. Burghoff, M. Will, S. Nolte, A. Tünnermann, Inscription of optical waveguides in crystalline silicon by mid-infrared femtosecond laser pulses, Opt Lett. 30 (9) (2005) 964–966.

[17] R. Wu, H. Liu, H. Yang, F. Chen, Q. Hu, H. Guo, Z. liu, Q. He, C. Zhang, Heterojunction-type hydrogen sensor based on silicon nanoconvexity induced by femtosecond laser, ACS Appl. Nano Mater. 6 (15) (2023) 13994–14002.
[18] M. Wu, N. Xu, E. Wang, S. Gen, H. Zhu, C. Liu, J. Cao, Nanogratings fabricated by wet etching assisted femtosecond laser modification of silicon for surface plasmon resonance sensing, Appl. Surf. Sci. 603 (2022) 154446.
[19] B. Wu, Y.C. Shin, A simplified predictive model for high-fluence ultra-short pulsed laser ablation of semiconductors and dielectrics, Appl. Surf. Sci. 255 (9) (2009) 4996–5002.
[20] A.E. Kaloyeros, Y. Pan, J. Goff, B. Arkles, Review-silicon nitride and silicon nitride-rich thin film technologies: state-of-the-art processing technologies, properties, and applications, ECS J. Solid State Sci. Technol. 9 (6) (2020) 63006.
[21] N. Hegedüs, K. Balázsi, C. Balázsi, Silicon nitride and hydrogenated silicon nitride thin films: a review of fabrication methods and applications, Materials (2021).
[22] A. Kaushik, H. Kahn, A.H. Heuer, Wafer-level mechanical characterization of silicon nitride MEMS, J. Microelectromech. Syst. 14 (2) (2005) 359–367.
[23] N. Sharma, M. Hooda, S.K. Sharma, Synthesis and characterization of LPCVD polysilicon and silicon nitride thin films for MEMS applications, J. Mater. (1) (2014) 954618, 2014.
[24] G. Verma, K. Mondal, A. Gupta, Si-based MEMS resonant sensor: a review from microfabrication perspective, Microelectron. J. 118 (2021) 105210.
[25] S. Sharma, N. Kohli, J. Brière, F. Nabki, M. Ménard, Integrated 1 × 3 MEMS silicon nitride photonics switch, Opt. Express 30 (12) (2022) 22200–22220.
[26] P.G. Kuzmin, G.A. Shafeev, V.V. Bukin, S.V. Garnov, C. Farcau, R. Carles, B. Warot-Fontrose, V. Guieu, G. Viau, Silicon nanoparticles produced by femtosecond laser ablation in ethanol: size control, structural characterization, and optical properties, J. Phys. Chem. C 114 (36) (2010) 15266–15273.
[27] S. Yang, W. Cai, H. Zeng, X. Xu, Ultra-fine β-SiC quantum dots fabricated by laser ablation in reactive liquid at room temperature and their violet emission, J. Mater. Chem. 19 (38) (2009) 7119–7123.
[28] X. Yu, S. Terakawa, S. Hayashi, T. Asaka, F. Itoigawa, S. Ono, J. Takayanagi, Carbonization of silicon nanoparticles via ablation induced by femtosecond laser pulses in Hexane, Arabian J. Sci. Eng. 42 (10) (2017) 4221–4226.
[29] S. Tóth, P. Németh, P. Rácz, L. Himics, P. Dombi, M. Koós, Silicon carbide nanocrystals produced by femtosecond laser pulses, Diam. Relat. Mater. 81 (2018) 96–102.
[30] S. Hammouti, B. Holybee, W. Zhu, J.P. Allain, B. Jurczyk, D.N. Ruzic, Titanium nitride formation by a dual-stage femtosecond laser process, Appl. Phys. A 124 (6) (2018) 411.
[31] R. Fedorov, F. Lederle, M. Li, V. Olszok, K. Wöbbeking, W. Schade, E.G. Hübner, Formation of titanium nitride, titanium carbide, and silicon carbide surfaces by high power femtosecond laser treatment, Chem. Plus Chem. 86 (9) (2021) 1231–1242.
[32] M. Worch, H.J. Engelmann, W. Blum, E. Zschech, Cross-sectional thin film characterization of Si compounds in semiconductor device structures using both elemental and ELNES mapping by EFTEM, Thin Solid Films 405 (1) (2002) 198–204.
[33] H. Dalaker, M. Tangstad, Temperature dependence of the solubility of nitrogen in liquid silicon equilibrated with silicon nitride, Mater. Trans. 50 (11) (2009) 2541–2544.
[34] X. Ma, C. Li, F. Wang, W. Zhang, Thermodynamic assessment of the Si–N system, Calphad 27 (4) (2003) 383–388.
[35] X. Chun-fang, H.A.N. Bing, Preparation of porous silicon nitride ceramics by microwave sintering and its performance evaluation, J. Mater. Res. Technol. 8 (6) (2019) 5984–5995.
[36] S. Hampshire, Fundamental aspects of hard ceramics, Comprehensive Hard Materials2014, pp. 3-28. .
[37] A. Zerr, G. Miehe, G. Serghiou, M. Schwarz, E. Kroke, R. Riedel, H. Fueß, P. Kroll, R. Boehler, Synthesis of cubic silicon nitride, Nature 400 (6742) (1999) 340–342.
[38] S.K. Biswas, The reaction of nitrogen gas with molten silicon, High-Pressure High-Temperat. 12 (1) (1980) 81–84.
[39] B.V. Stepanov, A.S. Mukasyan, K.G. Shkadinskii, Macrokinetics of $Si3_N4$Formation with gas transport of silicon, dokl, Phys. Chem. 302 (1) (1988) 145–149.
[40] A.S. Mukas'yan, B.V. Stepanov, Y.A. Gal'chenko, I.P. Borovinskaya, Mechanism of structure formation of silicon nitride with combustion of silicon in nitrogen, Combust. Explos. Shock Waves 26 (1) (1990) 39–45.
[41] S.V. Shabanov, I.B. Gornushkin, Modeling chemical reactions in laser-induced plasmas, Appl. Phys. A 121 (3) (2015) 1087–1107.
[42] A. Dmytruk, D. Proskuriakov, A. Karlash, M. Dmytruk, I. Dmytruk, V. Kadan, I. Blonskyi, M. Bondar, Polarization and kinetics of optical emission during laser induced periodic surface structure formation on crystalline silicon, Opt Laser. Technol. 177 (2024) 111073.
[43] J. Luo, C. Zhou, Q. Li, Y. Cheng, L. Liu, Diffusion coefficients of carbon, oxygen and nitrogen in silicon melt, J. Cryst. Growth 580 (2022) 126476.
[44] C. Florian, D. Fischer, K. Freiberg, M. Duwe, M. Sahre, S. Schneider, A. Hertwig, J. Krüger, M. Rettenmayr, U. Beck, A. Undisz, J. Bonse, Single femtosecond laser-pulse-induced superficial amorphization and Re-Crystallization of silicon, Materials (2021).
[45] T.H.R. Crawford, J. Yamanaka, G.A. Botton, H.K. Haugen, High-resolution observations of an amorphous layer and subsurface damage formed by femtosecond laser irradiation of silicon, J. Appl. Phys. 103 (5) (2008) 053104.